



HAL
open science

Sub 20 nm Upconversion Photosensitizers for Near-Infrared Photodynamic Theranostics

Anne Nsubuga, Korentin Morice, Nour Fayad, Federico Pini, Véronique Josserand, Xavier Le Guével, Abdallah Alhabi, Maxime Henry, Dario Puchan Sanchez, Nathan Plassais, et al.

► **To cite this version:**

Anne Nsubuga, Korentin Morice, Nour Fayad, Federico Pini, Véronique Josserand, et al.. Sub 20 nm Upconversion Photosensitizers for Near-Infrared Photodynamic Theranostics. *Advanced Functional Materials*, 2024, pp.2410077. 10.1002/adfm.202410077 . hal-04646350

HAL Id: hal-04646350

<https://hal.science/hal-04646350v1>

Submitted on 9 Oct 2024

HAL is a multi-disciplinary open access archive for the deposit and dissemination of scientific research documents, whether they are published or not. The documents may come from teaching and research institutions in France or abroad, or from public or private research centers.

L'archive ouverte pluridisciplinaire **HAL**, est destinée au dépôt et à la diffusion de documents scientifiques de niveau recherche, publiés ou non, émanant des établissements d'enseignement et de recherche français ou étrangers, des laboratoires publics ou privés.



Distributed under a Creative Commons Attribution 4.0 International License

Sub 20 nm Upconversion Photosensitizers for Near-Infrared Photodynamic Theranostics

Anne Nsubuga, Korentin Morice, Nour Fayad, Federico Pini, Véronique Josserand, Xavier Le Guével, Abdallah Alhabi, Maxime Henry, Dario Puchán Sánchez, Nathan Plassais, Pierre Josse, Julien Boixel, Philippe Blanchard, Clément Cabanetos,* and Niko Hildebrandt*

Efficient type II photodynamic therapy (PDT) requires stable and biocompatible photosensitizers (PS) that present low dark cytotoxicity, are photo-excitabile in deep tissue regions, and can efficiently penetrate and kill cells via in situ singlet oxygen production. Here, heavy-metal-free organic PS are combined with near-infrared (NIR)-excitable small (<20 nm) upconversion nanoparticles (UCNPs) into UCNP-PS nanohybrids for accomplishing such advanced PDT conditions. UCNP-to-PS energy transfer efficiencies between 11% and 42% and $^1\text{O}_2$ generation quantum yields between 74% and 86% resulted in efficient NIR-sensitized PDT. HeLa cells incubated with UCNP-PS can be efficiently destroyed via 808 nm laser irradiance at 140 mW cm^{-2} for 3 min (<30% cell viability) or 3.2 W cm^{-2} for 6 min (<10% cell viability). Theranostic functionality of UCNP-PS is demonstrated via live cell in situ imaging of intracellular UCNP-PS-mediated $^1\text{O}_2$ production, which resulted in cell death, most probably via apoptosis. Preliminary in vivo experiments are also performed and the consequences for a detailed in vivo study toward clinical translation are discussed. The combined PDT and deep-tissue imaging properties of the nanomolecular PS present a large potential for future implementation into advanced in vivo photodynamic theranostics.

1. Introduction

Photodynamic therapy (PDT) is a non-invasive technique that combines high therapeutic efficacy with minimal side effects for various types of cancer.^[1,2] The main process of PDT involves light-triggered generation of intracellular reactive oxygen species (ROS) via photosensitizers (PS) to induce cell death through apoptosis and necrosis.^[3,4] Ideal PS exhibits negligible dark cytotoxicity and efficient photoactivation into a long-lived excited triplet state (T1) via intersystem crossing (ISC) from an excited singlet state. From the T1, PS can subsequently undergo photochemical reactions yielding ROS, such as ROOH, OH $^{\bullet}$, and O $_2^{\bullet-}$ (type I process), or transfer their energy to molecular oxygen resulting in the (photo)generation of singlet oxygen ($^1\text{O}_2$, type II process).^[5-7] Both types of PDT have pros and cons. Type I is effective in hypoxic environments since it minimally

A. Nsubuga, N. Fayad, F. Pini
Univ Rouen, CNRS, INSA Rouen, Normandie Université
Laboratoire COBRA
Rouen 76000, France

K. Morice, D. Puchán Sánchez, N. Plassais, P. Josse, P. Blanchard,
C. Cabanetos
Univ Angers, CNRS, MOLTECH-ANJOU
SFR MATRIX
Angers 49000, France
E-mail: clement.cabanetos@univ-angers.fr

F. Pini
Istituto di Chimica della Materia Condensata e Tecnologie per l'Energia
(ICMATE)
Consiglio Nazionale delle Ricerche (CNR)
Padova 35131, Italy

 The ORCID identification number(s) for the author(s) of this article can be found under <https://doi.org/10.1002/adfm.202410077>

© 2024 The Author(s). Advanced Functional Materials published by Wiley-VCH GmbH. This is an open access article under the terms of the [Creative Commons Attribution](https://creativecommons.org/licenses/by/4.0/) License, which permits use, distribution and reproduction in any medium, provided the original work is properly cited.

DOI: 10.1002/adfm.202410077

F. Pini
Dipartimento di Scienze Chimiche
Università di Padova
Padova 35131, Italy

V. Josserand, X. Le Guével, A. Alhabi, M. Henry
University of Grenoble Alpes, Institute for Advanced Biosciences
INSERM-U 1209/CNRS-UMR5309
Grenoble 38700, France

J. Boixel
Univ Rennes
CNRS UMR6226
Rennes F-35042, France

C. Cabanetos
Building Blocks for Future Electronics Laboratory (2BFUEL), IRL CNRS
2002

Yonsei University
Seoul 03722, South Korea

N. Hildebrandt
Department of Chemistry
Seoul National University
Seoul 08826, South Korea
E-mail: hildebrandt@mcmaster.ca

depends on intracellular oxygen to produce ROS. The generation of multiple ROS can also decrease the likelihood of cells developing resistance to the therapy. Type II offers advantages in terms of specificity and selectivity, making it efficient in well-oxygenated tumors and tissues. Because $^1\text{O}_2$ has a very short lifetime, its diffusion distance is limited. Therefore, its effects are highly localized to the targeted area, reducing the risk of damaging surrounding healthy tissues.

Many PS, including organic dyes (e.g., porphyrins, Rose Bengal, zinc phthalocyanine, Chlorin e6, merocyanine 540, methylene blue) and metal-organic complexes, have been investigated as photoactive compounds in PDT for cancer treatment.^[8–12] However, significant drawbacks, such as high energy ultraviolet-visible (UV–vis) excitation light with low tissue-penetration depth, long-term toxicity due to slow metabolism processes, and low ISC efficiencies, have limited the efficacy and clinical translation of most of those PS.^[13,14] Considering that high ISC efficiencies are paramount for ROS generation, heavy atoms, such as halogens, transition metals, or lanthanides have been introduced in the π -conjugated system of the PS.^[13–16] This strategy increases spin–orbit coupling, which promotes ISC and leads to higher ROS production quantum yields. However, heavy atom-based PS can induce significant dark cytotoxicity causing genomic instability upon accumulation in the nucleus.^[13,17–19] In this context, the development of efficient heavy-atom-free molecular PS has recently attracted considerable research attention and still remains an important challenge.

Recently, Cabanetos et al. developed a new class of DNA binding heavy-atom free PS, entitled dibenzothioxanthene imide (DBI). DBI was demonstrated to interact with G-quadruplex secondary structures contained in exosomes of cancer cells.^[17] As a result, photoactivation (at 470 nm) of nanomolar concentration of DBI caused oxidative stress and DNA base degradation in both cancer cells and 3D tumor organoids. In vivo studies showed that DBI caused apoptosis in zebrafish, particularly in the area where it accumulated. In parallel, Cabanetos et al. also converted a benzothioxanthene imide chromophore into thiochromenocarbazole imide (TCI) with improved properties for electroluminescent devices.^[20,21] Characterized by high molar absorption coefficients, efficient ISC, and a long-lived T1, the *N*-annulated TCI showed great potential for being used as PS for $^1\text{O}_2$ generation.^[20] Moreover, the nitrogen-containing five-membered ring of TCI allowed for an orthogonal functionalization to the imide, therefore improving the tunability of the physicochemical, self-assembling, and grafting properties of this photoactive compound. Considering the advanced properties of both DBI and TCI, it would be highly interesting to i) experimentally verify the PS potential of TCI and ii) shift the UV–vis excitation of both derivatives into the near-infrared (NIR) for deeper tissue penetration and reduced water absorption.

Although red/NIR (up to circa 800 nm) excitable PS based on organic molecules and aggregation-induced emitters (AIEs) have been developed,^[18,22–24] they possess certain drawbacks, such as

photobleaching and lack of dual-modality (PDT plus luminescence imaging)^[25] for organic molecules and molecular-packing-dependent emission and broad emission bands for AIEs. Functionalization of both DBI or TCI for NIR excitation is chemically very challenging, but indirect excitation via upconversion nanoparticles (UCNPs) appears to be a method of choice.^[26–29] UCNPs can be excited in the NIR and produce UV–vis photoluminescence (PL), which is conducive to energy transfer to molecular PS near their surface.^[30–32] Thus, in principle, this concept should be transposable to the heavy-atom free DBI and TCI. The unique photophysical properties of UCNPs and their low toxicity make them also ideal candidates for various biological applications.^[33–40] Moreover, their versatile composition can be used to either excite Yb³⁺ sensitizers \approx 980 nm or Nd³⁺ sensitizers \approx 800 nm, where water absorption is weaker and heating effects can be avoided.^[40–46]

With the aim to develop ideal PS, we merged sub-20 nm UCNPs with DBI or TCI derivatives into single hybrid nanostructures for PDT (**Figure 1**). To do so, NaGdF₄:Nd³⁺/Tm³⁺/Yb³⁺@NaGdF₄ core-shell UCNPs excitable at 808 and 980 nm were coated with a phospholipid bilayer (PLB) for improved stability, biocompatibility, and encapsulation of both organic PS. Compared to previously demonstrated UCNP-to-PS materials,^[47–51] the combined advantages of our study were the use of heavy-atom free PS, excitation at 808 nm for less heat damage, small size (sub-20 nm), and an experimental investigation of the energy transfer process for a better fundamental understanding. The UV–vis PL of the UCNPs allowed for efficient Förster resonance energy transfer (FRET) to DBI and TCI in the PLB, which resulted in photosensitized $^1\text{O}_2$ production upon NIR excitation. In addition to evaluating the differences between the two different PS when they are incorporated into the PLB (aliphatic-DBI and hexyl-TCI), we also assessed the differences between incorporation into the PLB (hexyl-TCI) and direct attachment to the UCNP surface (maleimide-TCI) because variations of attachment ratios (PS-per-UCNP) and PS-to-UCNP distances should also result in distinct $^1\text{O}_2$ production efficiencies. Our characterization showed high $^1\text{O}_2$ production quantum yields and negligible dark toxicity of all three nanohybrids. Application to PDT was investigated through in vitro testing on human cervical cancer (HeLa) cell lines. As demonstrated by PL microscopy, UCNP-PLB-DBI/TCI nanohybrids were internalized by HeLa cells and NIR excitation resulted in an efficient PDT effect via intracellular $^1\text{O}_2$ production, highlighted by cell viability and cytotoxicity tests as well as live-cell imaging. Our results show that the synergistic combination of UCNPs and DBI/TCI resulted in powerful PS nanoplatforms with improved intracellular $^1\text{O}_2$ production for high therapeutic efficacy and minimal side effects. In addition, the NIR luminescence of the UCNP-PS can be used for simultaneous imaging with deep tissue penetration making them promising agents for photodynamic theranostics (PDTx).

2. Results and Discussion

2.1. Syntheses and Characterization of the Organic Photosensitizers

Three heavy-atom-free PS (aliphatic-DBI: *A-DBI*; hexyl-TCI: *H-TCI*; maleimide-TCI: *M-TCI*, **Figure 2**) were prepared following

N. Hildebrandt
McMaster University
Department of Engineering Physics
Hamilton, ON M8S 4K1, Canada

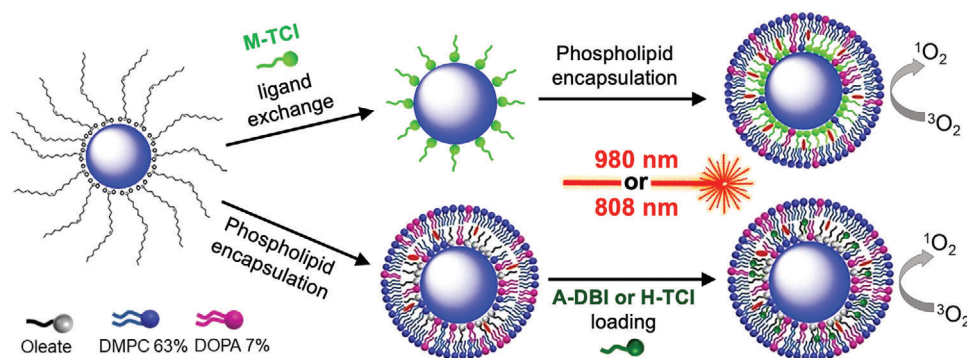


Figure 1. Schematic principle of the UCNP-PLB-PS nano platform for NIR-based PDTx. The different PS can be either directly attached to the UCNP surface and coated with PLB afterward (top) or incorporated in the PLB coated on the UCNP (bottom). NIR excitation of UCNPs with 980 or 808 nm results in UCNP-to-PS FRET and concomitant $^1\text{O}_2$ production.

recently reported procedures (see Supporting Information including Scheme S1 and Figures S1–S17 (Supporting Information) for synthetic details).^[17,20,21] The specifically designed PS allowed for different attachment approaches to the UCNPs and provided different photophysical properties for tuning UCNP-to-PS FRET. All three were found to have remarkably high solubility in common organic solvents, such as chloroform (CHCl_3), dichloromethane (DCM), dimethylsulfoxide (DMSO), and acetonitrile (ACN). The *N*-maleimide and *N*-hexyl moieties of TCI provided an additional pair of nonbonding electrons from the nitrogen atom, which induced a slight electron-donating effect to the π -system of the TCI chromophore.^[20,52] UV-vis absorption spectra (Figure 3) of H-TCI and M-TCI exhibited vis-centered absorption bands at circa 405 and 485 nm associated to molar extinction coefficients of ≈ 17000 and $\approx 16800 \text{ M}^{-1} \text{ cm}^{-1}$, respectively. Steady-state fluorescence spectroscopy showed H-TCI and M-TCI emission maxima at 521 and 526 nm, respectively (Figure S18, Supporting Information). A-DBI exhibited a singlet state absorption band at 483 nm, characterized by an extinction coefficient of $\approx 18000 \text{ M}^{-1} \text{ cm}^{-1}$ and an emission maximum at 544 nm, due to its fused and π -extended core. $^1\text{O}_2$ production quantum yields (Φ_s , indirect estimation of triplet generation efficiency) were determined at specific wavelengths by a relative method (Figure S19, Supporting Information) using phenalene ($\Phi_s = 0.95$ in CHCl_3) and Rose Bengal ($\Phi_s = 0.45$ in CH_3CN) as reference standards. The $^1\text{O}_2$ production quantum yields of $\Phi_s(\text{A-DBI}) = 0.86$, $\Phi_s(\text{H-TCI}) = 0.74$, and $\Phi_s(\text{M-TCI}) = 0.79$ were significantly higher than those of other heavy-atom-

free PS, such as BODIPY ($\Phi_s = 0.55$), thiol-based Nile Red ($\Phi_s = 0.36$), or thio-coumarin ($\Phi_s = 0.64$).^[18,53]

2.2. UCNP Production and Characterization

The material composition of the NaGdF_4 : 25% Yb^{3+} , 1% Nd^{3+} , 0.5% Tm^{3+} UCNPs was adapted for specific excitation at both 808 nm (Nd^{3+} ions) and 980 nm (Yb^{3+} ions) and emission in the 450–500 nm region (Tm^{3+} ions) that efficiently overlapped with the absorption of all organic PS (Figure 3). In addition to spectral overlap, FRET requires a close distance between the Tm^{3+} donors and the heavy-atom-free PS acceptors and a high PL quantum yield of the Tm^{3+} donors.^[43,54] Therefore, we prepared relatively small UCNPs with thin inert NaGdF_4 shells that presented a good compromise between bright (reduced surface quenching) donor PL and short (thin shell) donor-acceptor distances (see Supporting Information for experimental details).^[43,55] Small UCNP sizes were accomplished by using NaGdF_4 as a host material^[56–58] and by carefully adapting the ion ratios (185.5 mg $\text{GdCl}_3 \cdot 6\text{H}_2\text{O}$, 189.9 mg $\text{YbCl}_3 \cdot 6\text{H}_2\text{O}$, 3.8 mg $\text{NdCl}_3 \cdot 6\text{H}_2\text{O}$, and 3.8 mg $\text{TmCl}_3 \cdot 6\text{H}_2\text{O}$ —see Supporting Information for details).^[59,60] Dynamic light scattering (DLS) measurements of both core and core-shell UCNPs indicated an increase in the hydrodynamic diameter, from 11.8 ± 2.6 to 13.1 ± 3.1 nm, implying a shell thickness of circa 1.5 nm (Figure S20A,B, Supporting Information). Sizes as well as a narrow distribution (12.4 ± 2 nm) and excellent monodispersity were

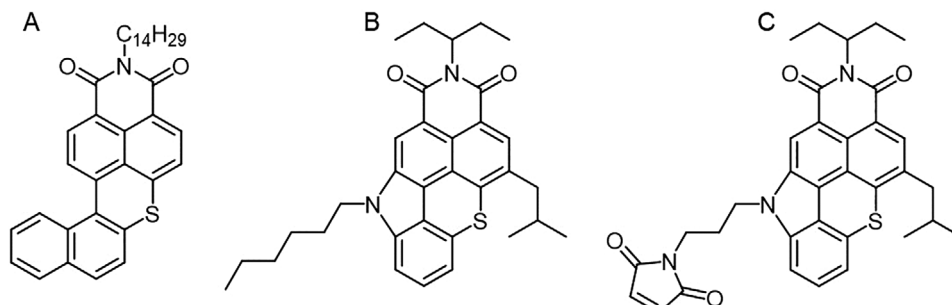


Figure 2. Chemical structures of A-DBI (A), H-TCI (B), and M-TCI (C) Synthetic routes are provided in Scheme S1 (Supporting Information).

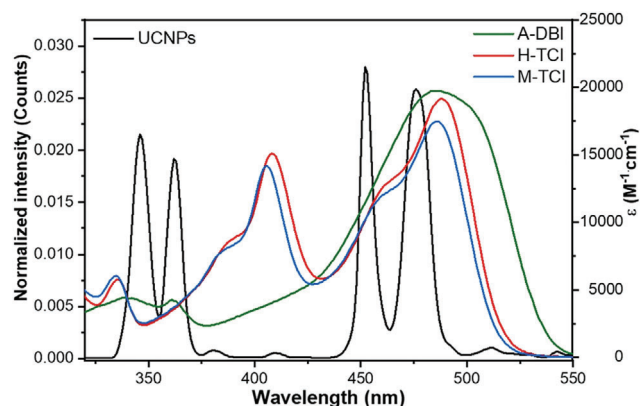


Figure 3. The spectral overlap of UCNPs PL ($\lambda_{\text{ex}} = 808$ nm, black line, left axis) and molar extinction coefficient spectra of the three PS (green, blue, and red lines, right axis) is optimal for UCNPs-to-PS FRET.

confirmed by transmission electron microscopy (TEM, Figure S20C, Supporting Information). Powder X-ray diffraction experiments (Figure S20D, Supporting Information) revealed that the core-shell UCNPs were in the thermodynamically stable hexagonal phase without phase impurities. Regarding their optical properties, the UCNPs PL spectrum (Figure 3) displayed the characteristic and expected emission bands of Tm^{3+} . The UV emission bands at ≈ 353 and ≈ 368 nm were assigned to the ${}^3\text{P}_0 \rightarrow {}^3\text{F}_4$, and ${}^1\text{D}_2 \rightarrow {}^3\text{H}_6$ transitions, respectively. The blue emission bands at ≈ 456 and ≈ 481 nm were assigned to the ${}^1\text{D}_2 \rightarrow {}^3\text{F}_4$ and ${}^1\text{G}_4 \rightarrow {}^3\text{H}_6$ transitions, respectively. Tm^{3+} also exhibits emission bands beyond 500 nm (e.g., ≈ 650 , ≈ 690 , and ≈ 800 nm) but since they do not overlap with the PS' absorption, most of them are deliberately not shown in the PL spectrum in Figure 3. An energy level diagram showing the most important optical transitions is provided in Figure S21 (Supporting Information).

2.3. FRET Parameters

The spectral overlap integrals ($J(\lambda)$) of the three UCNPs-PS FRET pairs were calculated between 320 and 550 nm using Equation (1):

$$J(\lambda) = \int \bar{I}_D(\lambda) \epsilon_A(\lambda) \lambda^4 d\lambda \quad (1)$$

where, $\bar{I}_D(\lambda)$ is the normalized intensity ($\int \bar{I}_D(\lambda) d\lambda = 1$) of Tm^{3+} emission in the 320 to 550 nm range (the other transitions were not considered for the normalization), $\epsilon_A(\lambda)$ is the molar extinction coefficient (in $\text{M}^{-1} \text{cm}^{-1}$) of the acceptor, and λ is the wavelength in nm. Overlap integral values of $J(\text{A-DBI}) = 5.2 \cdot 10^{14} \text{ M}^{-1} \text{cm}^{-1} \text{nm}^4$, $J(\text{H-TCI}) = 4.4 \cdot 10^{14} \text{ M}^{-1} \text{cm}^{-1} \text{nm}^4$ and $J(\text{M-TCI}) = 4.2 \cdot 10^{12} \text{ M}^{-1} \text{cm}^{-1} \text{nm}^4$ were used to estimate Förster distances (corresponding to the distance between donor and acceptor that results in 50% FRET efficiency) by Equation (2):

$$R_0 = 0.021 (\kappa^2 \Phi_D n^{-4} J)^{1/6} \times \text{nm} \quad (2)$$

κ^2 is the donor-acceptor transition dipole moment orientation factor, which we assumed to be $2/3$ due to dynamic averaging during the long excited-state lifetime of the Tm^{3+} donors. Φ_D is

the PL quantum yield of the Tm^{3+} donors, which is difficult to determine since it is different from the overall quantum yield of the UCNPs. Therefore, R_0 values were calculated with donor quantum yields of 0.1%, 1%, and 10%, which provided a range estimation of R_0 . Further, a refractive index of $n = 1.35$ (aqueous buffer) was used. The Förster distances for all three FRET pairs were found to be in the 1.4 to 3.1 nm range. While the exact R_0 values are of minor importance, the distance range emphasizes that Tm ion donors, located in the core of the UCNPs, and PS acceptors, located on the surface of the inert UCNPs shell, should be as close as possible to accomplish sufficient UCNPs-to-PS FRET. This distance consideration is one of the main reasons for the relatively thin inert shell and the different PS surface attachment approaches discussed below.

2.4. UCNPs-PS Preparation and Characterization

To stabilize the aliphatic functionalized PS (A-DBI or H-TCI) close to the UCNPs surface and to maximize biocompatibility and stability for in vitro imaging and PDTx applications, UCNPs were coated with phospholipids using thin-film hydration (molar ratio 0.63/0.3/0.07 1,2-dimyristoyl-sn-glycero-3-phosphocholine (DMPC)/cholesterol/1,2-dioleoyl-sn-glycero-3-phosphate (DOPA), see Supporting Information for experimental details).^[61] Whereas different surface coating strategies can be used for encapsulating UCNPs and incorporating small molecules, we selected phospholipids because they provide similar properties than cell membranes combined with high stability, biocompatibility, and encapsulation efficiency.^[32,62,63] In a typical experiment, a dispersion of UCNPs (3 mg mL^{-1} in chloroform) was first added to a solution of phospholipids and cholesterol in chloroform before drying the reaction mixture to form a thin film (60 min at 50°C). The film was then hydrated with 4-(2-hydroxyethyl)-1-piperazineethanesulfonic acid (HEPES) buffer and sonicated to generate stable and dispersible UCNPs-PLB. Thermal gravimetric analysis showed a weight loss of circa 9% (Figure S22, Supporting Information), representing $3.8 \cdot 10^{17}$ oleate ligands per UCNPs and corresponding to a surface coverage of $\approx 76\%$, which corroborates the presence of DMPC in the inner leaflet driven by electrostatic interactions. DMPC was used to prevent repulsion between the negatively charged head groups of DOPA. Cholesterol was used to decrease water permeability, as it is known to create a tighter packing in lipid films comprising unsaturated fatty acid chains. A zeta potential of -11.2 mV was measured and DLS experiments confirmed the colloidal stability when incubated in water and phosphate-buffered saline (PBS) for up to 7 days (Table S1, Supporting Information).

Whereas A-DBI and H-TCI were encapsulated (thin-film hydration method in the dark) within the hydrophobic layers via hydrophobic interactions (between the lipid aliphatic bilayer and the PS), the maleimide functionalized M-TCI was grafted on the UCNPs surface before PLB coating. To do so, oleate ligands were first replaced with mercaptopropionic acid (MPA), through a ligand exchange reaction in acidic conditions, that, in turn, reacted with M-TCI through thiol-maleimide coupling. The surface modification process was monitored by Fourier transform infrared spectroscopy (Figure S23, Supporting Information).

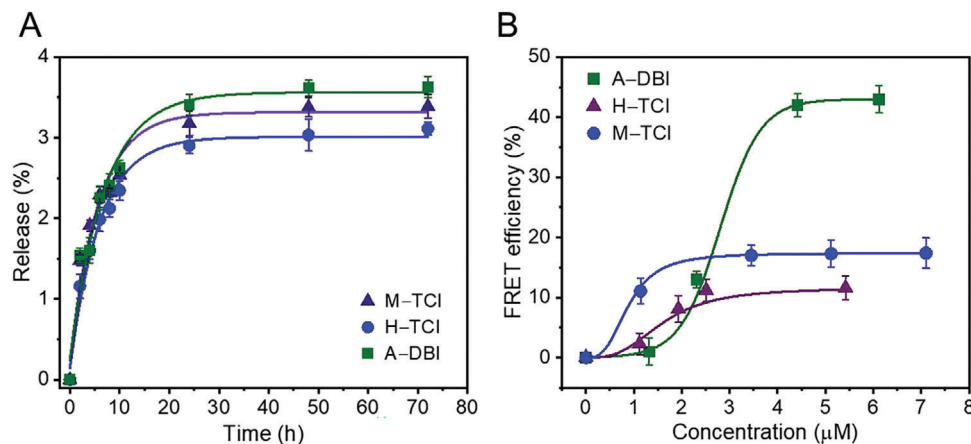


Figure 4. A: Time-dependent release of encapsulated PS in HEPES buffer (pH 5.4) at 37 °C. B: FRET efficiencies of UCNP-PLB-PS with increasing concentrations of PS. The error bars for each data point represent the standard deviation derived from three separate measurements ($n = 3$).

Different concentrations of M-TCI were studied to determine the optimum number per UCNP for high FRET efficiency and subsequent $^1\text{O}_2$ production. PLB coating was performed after M-TCI functionalization of MPA-UCNPs.

The stability of the UCNP-PS nanohybrids was first assessed by DLS, which showed that all UCNP-PS had very similar sizes and excellent colloidal stability for up to 7 days (Table S1, Supporting Information). PS release kinetics of A-DBI, H-TCI, and M-TCI were also evaluated. UCNP-PS were placed in a dialysis membrane (3,000 Da molecular weight cutoff) and the leakage of PS molecules was monitored at specific time intervals (i.e., up to 72 h) by UV-vis absorption spectroscopy. The hydrophobic interactions between PS and the PLB resulted in only minimal leakage (of less than 4%) within circa 20 h, after which no more leakage occurred (Figure 4A). The small differences between the plateau values of the three PS are not significant enough to explain it via the different structures or attachment procedures. The PS release was fitted to a single exponential function generating time constants of ≈ 9.8 h, ≈ 8.3 h, and ≈ 9.8 h for A-DBI, H-TCI, and M-TCI, respectively (Equation S1, Supporting Information), which represented the time to reach 50% of the plateau value. Overall, loading these rylene based PS into the hydrophobic PLB resulted in highly stable nanocarriers, which is critical for ensuring that the therapeutic load reaches the cancer cell targets.

2.5. UCNP-to-PS FRET

To determine the FRET efficiencies (E_{FRET}) from the UCNP to the different PS, the Tm^{3+} PL intensity in the overlapping spectral range, that is, from 320 to 550 nm (cf. Figure 3) was studied and Equation (3) applied:

$$E_{\text{FRET}} = 1 - \left(\frac{I_{\text{DA}}}{I_{\text{D}}} \right) \quad (3)$$

I_{DA} and I_{D} are the integrated UCNP PL intensities from 320 to 550 nm in the presence and in absence of the PS acceptors, respectively. Importantly, these overall FRET efficiencies considered the total UCNP PL intensity, which includes many Tm^{3+}

donors that were close to the center of the UCNP and could not participate in FRET to PS (too large Tm^{3+} -PS distance). Therefore, higher overall FRET efficiency can originate from both closer distance of the PS to the UCNP surface (higher FRET efficiencies for each existing FRET pair) and larger amounts of PS per UCNP (higher amount of FRET pairs). Increasing the concentration of each PS resulted in gradual quenching of the UCNP PL until a certain limit (Figure S24, Supporting Information). From these measurements, maximal FRET efficiencies of 0.42 ± 0.05 , 0.11 ± 0.03 , and 0.17 ± 0.03 were achieved at concentrations of 4.2 ± 0.6 , 3.0 ± 0.4 , and 2.1 ± 0.4 μM for A-DBI, H-TCI, and M-TCI, respectively (Figure 4B). Considering a UCNP concentration of 0.68 μM , PS-per-UCNP ratios were estimated as 6.2 ± 0.9 , 4.4 ± 0.6 , and 3.1 ± 0.6 for A-DBI, H-TCI, and M-TCI, respectively (see Supporting Information for details about the calculations). Despite the lower PS-per-UCNP ratios for M-TCI compared to H-TCI, the closer PS-to-UCNP-surface distance, resulting from the chemical attachment to the UCNP (vide supra), yielded in a higher E_{FRET} (M-TCI). Knowing that both A-DBI and H-TCI should be localized inside the PLB and at approximately the same average distance from the UCNP surface, the higher E_{FRET} (A-DBI) can be correlated to a higher incorporation efficiency (higher PS-per-UCNP ratio). For the same reason, E_{FRET} (A-DBI) was also significantly higher than E_{FRET} (M-TCI) despite the closer distance of M-TCI to the UCNP surface.

Overall, E_{FRET} values between 11% and 42% were quite encouraging when considering that many Tm^{3+} FRET donor ions inside the UCNP were actually quite far away from the PS acceptors. These relatively large overall FRET efficiencies confirmed that the small UCNP diameters below 20 nm and the relatively compact surface attachment strategies were well selected for our NIR-activated and UCNP-sensitized PDT strategy. Importantly, we were able to directly observe the production of $^1\text{O}_2$ via its phosphorescence ≈ 1270 nm upon excitation of the UCNP-PS nanohybrids at 980 nm (Figure S26, Supporting Information). Whereas electron spin resonance or fluorescent probes can also be used for gaining experimental evidence of $^1\text{O}_2$ production, detection of $^1\text{O}_2$ phosphorescence is arguably the most direct way and we therefore did not employ additional methods. It is rare that this phosphorescence peak is measurable for $^1\text{O}_2$ production

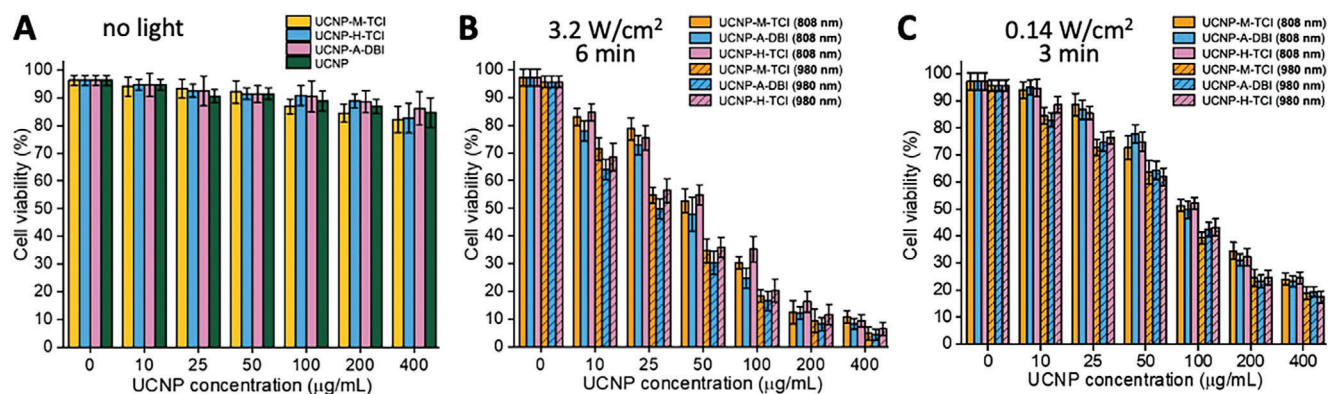


Figure 5. Cell viability of HeLa cells incubated for 20 h with different concentrations (0–400 $\mu\text{g}\cdot\text{mL}^{-1}$) of UCNP-PS. UCNP concentration-dependent MTT assays were performed without light irradiation (A), with strong (3.2 W cm^{-2} for 6 min) NIR excitation at 808 or 980 nm (B), and with moderate (0.14 W cm^{-2} for 3 min) NIR excitation at 808 or 980 nm (C). Error bars represent the relative standard deviation from triplicate measurements ($n = 3$). Note that “0” concentration corresponds to experiments without UCNPs. Thus, only one experiment (triplicate measurements) was performed for each excitation condition (no light, 808, and 980 nm). For clarity, all samples are shown for the “0” concentration in concentration experiments, which resulted in bars with the same cell viability and errors.

via UCNP-to-PS energy transfer upon NIR excitation and thus, our $^1\text{O}_2$ production can be considered as relatively efficient. Note that UCNP-PS collected by centrifugation were re-dispersed in D_2O to increase the $^1\text{O}_2$ lifetime and thereby enabling the detection of the weak $^1\text{O}_2$ phosphorescence.^[64]

2.6. In-Vitro Toxicity Assessment

Encouraged by the excellent FRET properties and NIR-activated $^1\text{O}_2$ production ability, the potential application of these nanocarriers for PDT and (bio)imaging was investigated. We were also very interested in assessing the relationship between FRET efficiencies and $^1\text{O}_2$ production efficiency. As mentioned above, the FRET efficiency was quantified via UCNP luminescence quenching. However, a stronger quenching of all Tm^{3+} ions within the UCNP (and thus higher overall FRET efficiency) does not necessarily represent the PS-sensitization and $^1\text{O}_2$ production efficiencies. Thus, it was important to scrutinize all three UCNP-PS concerning their potential NIR-induced cytotoxicity, which was done via in vitro cell viability tests using a standard 3-(4,5-dimethylthiazol-2-yl)-2,5-diphenyltetrazolium bromide tetrazolium (MTT) assay and HeLa human cervical cancer cells. HeLa cells were incubated with the nanohybrids at concentrations ranging from 10 to 400 $\mu\text{g}\cdot\text{mL}^{-1}$ for 20 h at 37° C followed by the replacement of cell media with fresh HBSS (see Supporting Information for experimental details).

In the absence of NIR irradiation, UCNP-PS incubated HeLa cells exhibited high viability between circa 86 and 93% (Figure 5A), emphasizing minimal dark-cytotoxicity of all three nano-PS. Control experiments with UCNP-PLB confirmed that the slightly increasing dark toxicity with increasing UCNP-PS concentrations was caused by the NPs and not by the PS (Figure 5A). Continuous and homogeneous irradiation of the cells (prior to MTT assays) at 980 and 808 nm with high power densities and for an extended time (3.2 W cm^{-2} for 6 min) and moderate power densities for a shorter time (0.14 W cm^{-2} for 3 min) resulted in much stronger and concentration-dependent

cytotoxicity with cell viabilities below 10% for the highest UCNP-PS concentration and strong excitation (Figure 5B). Moderate excitation still led to significant UCNP-PS concentration-dependent cytotoxicity (Figure 5C) but the influence of excitation irradiance and time was clearly visible (when comparing Figure 5B,C). Despite the differences in overall FRET efficiencies (vide supra) all three types of UCNP-PS induced approximately the same cytotoxicity. Taking into account that the $^1\text{O}_2$ production quantum yields of the three PS were very similar (vide supra), the similar cytotoxicities suggest that the overall sensitization of the three different PS via FRET from UCNPs was not significantly different. The slightly stronger PDT effect at 980 nm excitation was attributed to the direct excitation of Yb^{3+} sensitizer ions (absorption cross-section of $\approx 10^{-20}\text{ cm}^2$) and subsequent energy transfer to the Tm^{3+} activator ions.^[65] Despite the circa 10-fold higher absorption cross-section of Nd^{3+} ($\approx 10^{-19}\text{ cm}^2$) compared to Yb^{3+} , upconversion upon 808 nm excitation is less efficient as it results from $\text{Nd}^{3+} \rightarrow \text{Yb}^{3+} \rightarrow \text{Tm}^{3+}$ energy transfer.^[66] Nevertheless, both 808 and 980 nm excitation of UCNP-PS resulted in significantly reduced cell viability. Notably, NIR irradiation of HeLa cells without UCNP-PS did not lead to cytotoxic effects (compare bars at 0 UCNP concentration in Figure 5A–C).

2.7. Live-Cell Imaging and Cellular Uptake

To investigate cellular uptake and intracellular localization of the nanohybrids, live HeLa cells were incubated for 4 h with the different UCNP-PS and then counterstained with Hoechst 33342, a nuclei staining agent. To provide a good compromise between low dosing and high PDT efficacy, a UCNP-PS concentration of 100 $\mu\text{g}\cdot\text{mL}^{-1}$ was selected (cf. Figure 5B,C). Cellular uptake and intracellular localization of the PS-loaded NPs were visualized via widefield fluorescence microscopy. The overlay images of differential interference contrast (DIC) transmission, nucleus-specific Hoechst 33342 fluorescence, and UCNP luminescence (Figure 6) showed that all three types of UCNP-PS were internalized and mainly located within the cytoplasm of the HeLa

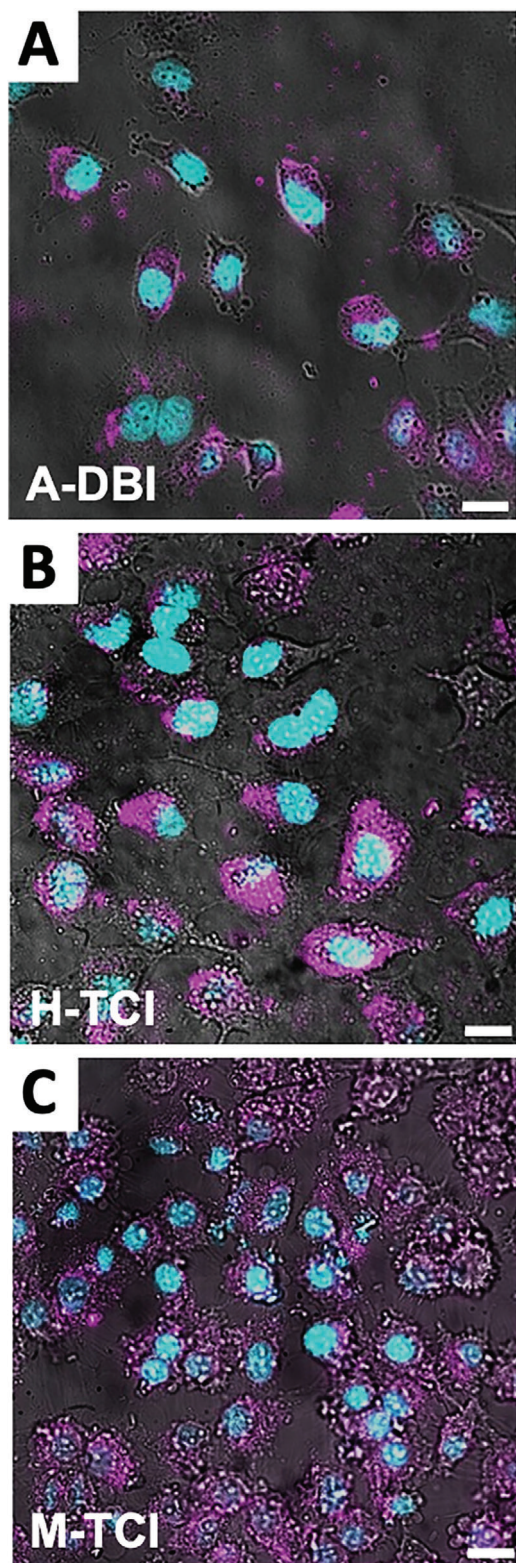


Figure 6. Overlay images (DIC transmission; Hoechst 33342 fluorescence in blue with 320 ± 20 nm excitation and 480 ± 8 nm emission detection; UCNP luminescence in magenta with 808 nm laser excitation and 450 ± 30 nm emission detection) of HeLa cells incubated for 4 h with $100\ \mu\text{g mL}^{-1}$ UCNP-A-DBI (A), UCNP-H-TCI (B), and UCNP-M-TCI (C). Scale bars: 20 μm .

cells. Consequently, the cell toxicity demonstrated above was most probably induced by UCNP-PS inside the cells, that is, $^1\text{O}_2$ -induced apoptosis leading to cell rupture and subsequent cell death.^[67,68]

For assessing the dose-dependent toxicities and intracellular distribution at the single-cell level, microinjection of well-controlled sample volumes into single cells is an interesting delivery method.^[69,70] However, clogging of the sample via NP aggregation in the extremely thin delivery needles can present a significant limitation for microinjection.^[71] Thus, we wanted to demonstrate that the UCNP-PS nanohybrids can be used for microinjection and subsequently imaged inside the cells. Direct microinjection into the cytoplasm of live COS-7 cells without inducing cell rupture and needle clogging was successfully carried out for up to ≈ 9.2 pL of UCNP-PS. Imaging revealed that UCNP-PS were relatively well distributed despite a certain localization (Figures S27 and S28, Supporting Information), which could indicate slight aggregation within the cytoplasm or that a certain time is necessary to distribute the UCNP-PS over the entire cytosol (which is quite densely packed with subcellular components).

2.8. Intracellular $^1\text{O}_2$ Production via UCNP-PS

Considering that the overall FRET efficiency (measured via UCNP luminescence intensity) and the cytotoxicity (measured via cell viability assays) were not directly related, we aimed to analyze the actual $^1\text{O}_2$ production capability of UCNP-PS inside cells. For this, HeLa cells were incubated for 4 h with the different UCNP-PS ($100\ \mu\text{g mL}^{-1}$). Following the removal of non-internalized NPs by washing with HBSS, cells were excited with an 808 nm laser at $3.2\ \text{W cm}^{-2}$ for 6 min (Figure 7 left) or at $0.14\ \text{W cm}^{-2}$ for 3 min (Figure 7 right) in order to induce the production of intracellular $^1\text{O}_2$. For all three different UCNP-PS, the images clearly showed morphological changes of the cells, indicative of cell death. UCNPs inside the cells were still luminescent (upon both 980 and 808 nm excitation) and mainly localized in the cytosol. NIR-excitation of HeLa cells alone did not result in any detectable morphological change or damage (Figure S29, Supporting Information). Fluorescence imaging of calcein-AM and propidium iodide (PI) co-stained cells (for revealing live and dead cells) also confirmed the PDT efficacy of the NIR-excited UCNP-PS (Figure S30, Supporting Information). These results demonstrated the theranostic PDT applicability of this new class of hybrid nanostructures via simultaneous cell destruction and imaging.

To further verify that the cell damage was caused by the NIR excitation-induced production of $^1\text{O}_2$, as already shown via $^1\text{O}_2$ phosphorescence in solution (Figure S26, Supporting Information), the fluorescent $^1\text{O}_2$ probe *singlet oxygen sensor green* (SOSG) was used to stain HeLa cells (5 nM of SOSG for 10 min). Unlike other commercially available fluorescent and chemiluminescent ROS probes, SOSG is highly specific to $^1\text{O}_2$ and does not show any appreciable response to hydroxyl radical ($\text{OH}\cdot$) or superoxide (O_2^-). In the presence of $^1\text{O}_2$, SOSG produces an endoperoxide (SOSG-EP) resulting in strong fluorescence emission (excitation/emission maxima $\approx 485/525$ nm) (Figure 8B). Before 808 nm laser irradiation, the characteristic fluorescence

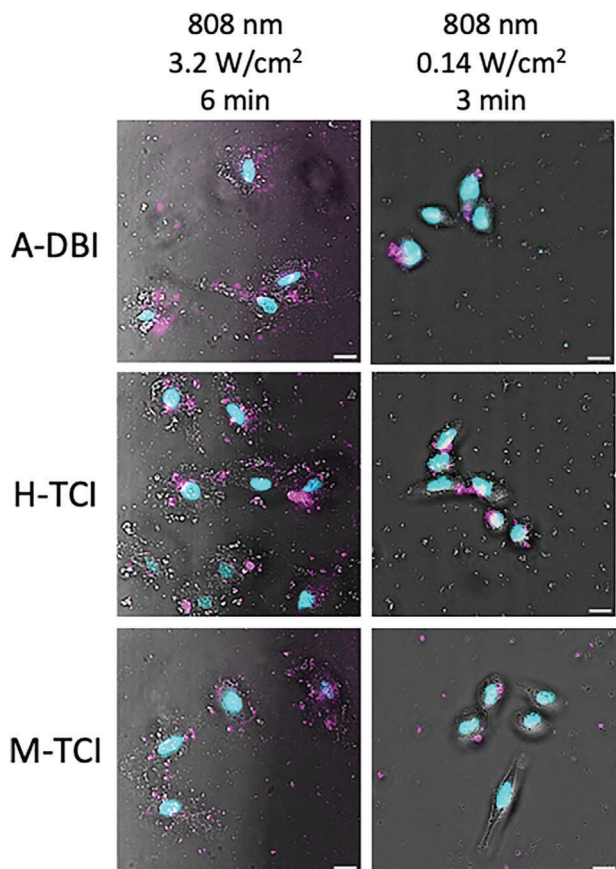


Figure 7. DIC-luminescence overlay (DIC transmission; HOECHST 33342 fluorescence in blue with 320 ± 20 nm excitation and 480 ± 8 nm emission detection; UCNP luminescence in magenta with 980 or 808 nm laser excitation and 450 ± 30 nm emission detection) images of live HeLa cells after 4 h of incubation with the three different UCNP-PS and subsequent 3 min $^1\text{O}_2$ production under intense NIR excitation (left, 808 nm, 3.2 W cm^{-2} , 6 min) and moderate NIR excitation (right, 808 nm, 140 mW cm^{-2} , 3 min). All scale bars are 20 μm . DIC images and results for 980 nm excitation are shown in Figure S31 (Supporting Information).

of SOSG in HeLa cells treated with UCNP-PS appeared very weak (Figure 8A bottom images). This negligible fluorescence was probably caused by oxidative stress as a result of the imbalance between ROS formed in cells and the inability of the biological systems to detoxify ROS species.^[5,72] Although antioxidant defense systems, such as catalase, superoxide dismutase, and glutathione peroxidase, regulate the homeostasis of ROS, detectable amounts of $^1\text{O}_2$ can be naturally present in cells. In strong contrast, a very intense green fluorescence was monitored in the cells after 808 nm irradiation (Figure 8A top images), suggesting a high level of intracellular $^1\text{O}_2$ production. The total fluorescence intensity inside the cells was quantified and showed relative increases of 7.5, 11, and 15 fold (after 808 nm irradiation with 3.2 W cm^{-2} for 6 min) or 3.5, 3.9, and 4.3 fold (after 808 nm irradiation with 140 mW cm^{-2} for 3 min) for UCNP-A-DBI, UCNP-H-TCI, and UCNP-M-TCI, respectively (Figure 8C). These results highlight that the oxidative stress (intracellular $^1\text{O}_2$ production) mediated via NIR excitation of UCNPs followed by FRET to PS led to efficient cell death, which further confirmed

the decrease in cell viability analyzed by MTT assays (cf. Figure 5). Interestingly, $^1\text{O}_2$ -induced fluorescence was most intense for the UCNP-M-TCI, followed by UCNP-H-TCI, and UCNP-A-DBI, which showed that careful analysis of all steps from NIR excitation, over FRET UCNP quenching, FRET-induced cytotoxicity, and intracellular FRET-induced $^1\text{O}_2$ production can reveal quite different results that are not necessarily directly related. It could well be that the closer distance of the M-TCI to the UCNP surface is the reason for the more intense $^1\text{O}_2$ production. However, our results rather indicate that a systematic investigation of UCNP-PS distances and PS incorporation strategies beyond our three PS will be necessary to fully understand how these parameters can be used to further optimize $^1\text{O}_2$ production and cytotoxicity. Obviously, stronger irradiation also resulted in higher $^1\text{O}_2$ production. But when considering that the final aim would be an in vivo clinical application, irradiation fluences are always limited to a maximum permissible skin exposure for safety reasons and for avoiding skin damage.

2.9. In-Vivo Study

Despite efforts to reduce and replace the use of animals in non-clinical research (e.g., FDA Modernization Act 3.0 – new legislation that was introduced in the U.S. House of Representatives on February 6th, 2024),^[73] in vivo experiments are still broadly considered as very important and impactful for nonclinical material development research. It is certainly true that clinical translation requires in vivo experiments at a certain stage but meaningful in vivo investigations are very time-consuming, require detailed assessment of pharmacokinetics, and should be well planned and conducted in separate studies. In particular, the demonstration of in vivo PDT therapeutic efficacy by using extremely high irradiances above the common safety and ethics standards is questionable. For 808 nm irradiation of the skin for more than 10s, European (EN60825) and American (ANSI Z136.1) standards suggest a maximum irradiance of circa 330 mW cm^{-2} . However, many 808 nm UCNP-based studies applied significantly higher irradiances and/or very long irradiation times of more than 30 min.^[40,74–76] For 980 nm, the safety regulation allows approximately double the irradiance, which is also somewhat strange when considering the higher tissue absorption of 980 nm compared to 808 nm light.^[77–79]

Although quite preliminary at this stage of material development and despite the possibly limited information to be gained, we wanted to evaluate if our UCNP-PS may already provide PDT efficacy in mice bearing subcutaneous tumor xenografts. We did not quantify the penetration depth in vivo as the superior tissue penetration of 808 nm was already demonstrated for various different tissues.^[77–79] To limit the animal experiments to the absolutely necessary, we only investigated UCNP-M-TCI, as those UCNP-PS provided the strongest intracellular $^1\text{O}_2$ production-specific fluorescence intensity increase (cf. Figure 8). We used the moderate irradiance of 140 mW cm^{-2} with a relatively short (3 min) irradiation time (corresponding to a fluence of circa 25 J cm^{-2}) to be within the safety regulations, not to cause damage to the skin, and to provide a margin for future applications on deeper tumors. 18 Naval Medical Research Institute (NMRI) nude mice were subcutaneously implanted with 10×10^6 HeLa

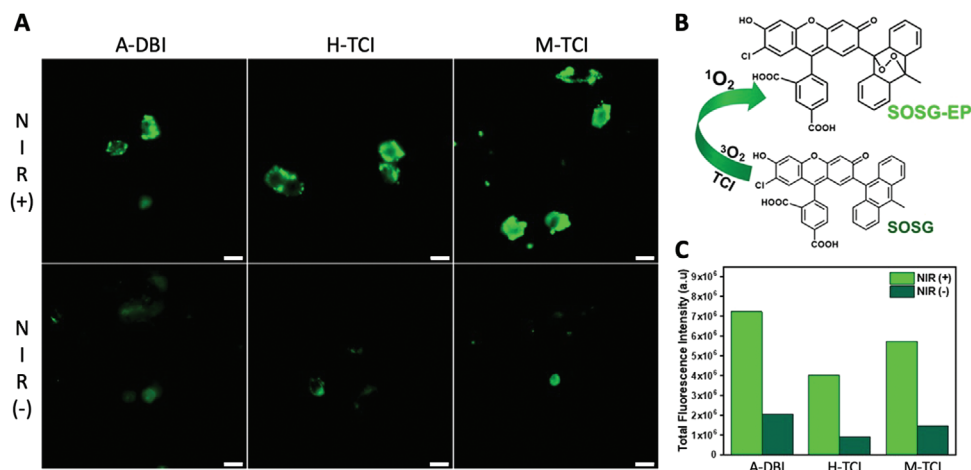


Figure 8. A: Intracellular generation of singlet oxygen ($^1\text{O}_2$) was detected in HeLa cells treated with UCNP-PS using green SOSG fluorescence after irradiation (top, NIR (+)) and before (bottom, NIR (-)) irradiation with an 808 nm laser for 3 min (140 mW cm^{-2}). B: $^1\text{O}_2$ -mediated chemical structure change of SOSG to SOSG-EP, resulting in green fluorescence. C: Green fluorescence intensities calculated from the images in A. Scale bars: 20 μm . Results for 808 nm irradiation at 3.2 W cm^{-2} for 6 min are shown in Figure S32 (Supporting Information).

cells (200 μL in PBS) on the right flank. When the tumor volumes reached at least 100 mm^3 , 12 mice received an intratumoral injection of 50 μL of 20 mg mL^{-1} UCNP-M-TCI and six mice received an intratumoral injection of 50 μL NaCl (0.9%). The 18 mice were then separated into three groups ($n = 6$), two of which were control groups. The tumors of one UCNP-M-TCI group and the NaCl group were illuminated (808 nm, 140 mW cm^{-2} , 3 min) 1 and 24 h after intratumoral injection, and the other UCNP-M-TCI group was not illuminated. Whereas the UCNP-M-TCI PL could be imaged in vivo, unfortunately, no significant effects on tumor growth were observed (see Supporting Information including Figures S31–S34, Supporting Information for detailed results), which confirmed our initial assessment that a separate and detailed in vivo study would be necessary for a more relevant evaluation. Considering that efficient intracellular $^1\text{O}_2$ production and cytotoxicity were experimentally demonstrated under the same illumination conditions via various approaches in vitro (vide supra), the different tumor microenvironment, a too-low irradiance, a too-short illumination time, or inhomogeneous accumulation of UCNP-M-TCI in the tumor due to the intratumoral injection (versus a possibly more homogeneous diffusion by intravenous injection) and concomitant reduced cellular uptake could be possible reasons for the lacking PDT effect.

Because a more detailed in vivo investigation was out of the scope of our current study, we focused on the lessons learned from the preliminary in vivo results with the aim to implement them in a detailed in vivo PDT assessment in the future. Although our sub-20 nm UCNP-PS already provided relatively efficient $^1\text{O}_2$ production upon 808 nm irradiation, there are still possibilities to make them even more efficient without making them larger. One route could be the replacement of the NaGdF_4 host material by LiGdF_4 or LiYbF_4 , which was shown to provide small and bright UCNPs.^[80–83] In addition to using more efficient UCNPs, a detailed in vivo study should investigate different irradiances and fluences, different UCNP-PS concentrations, intravenous injection, and more relevant tumor models. Using organoids as an intermediate step between 2D cell culture and

in vivo experiments would be another possibility to optimize the material conditions toward clinical translation.

3. Conclusion

PS with high PDT efficacy and low dark toxicity require the design of heavy-metal free molecules with strong light absorption and efficient ROS production. To also accomplish deep tissue penetration of the excitation light, NIR-excitable PS would be ideal. However, organic PS molecules can only be excited in the UV–vis spectral region. This drawback can be overcome by UCNPs, whose UV–vis emission (upon NIR excitation) can be used for FRET to organic PS close to their surfaces. This concept can in principle even be used for PDTx because the PL of the UCNP-PS nanohybrids can be imaged during the therapeutic effect. Whereas such a PDTx strategy can be easily established on a drawing board, the experimental implementation faces several interconnected challenges: i) heavy-metal free PS molecules must provide high $^1\text{O}_2$ production quantum yields; ii) these PS must be brought in very close and permanent proximity to the UCNP for efficient FRET; iii) at the same time, the PS must be in physical contact to the surrounding environment for efficient $^1\text{O}_2$ production; iv) the UCNPs must be well protected from the surrounding environment to avoid PL quenching; v) at the same time, the UCNP protection shell must be very thin to guarantee a close UCNP-to-PS distance for efficient FRET; vi) the UCNPs must be small, such that many emitting lanthanide donors can function as FRET donors and to afford efficient cellular penetration; vii) at the same time, the UCNPs must be sufficiently large to provide bright PL for imaging; viii) UCNP excitation at 808 nm is preferred over excitation at 980 nm to avoid heating due to light absorption by water; ix) at the same time, 808 nm excitable UCNPs are usually less bright than 980 nm excitable ones; x) the entire UCNP-PS nanohybrid must be biocompatible and stable; xi) at the same time, the biocompatible coating must not be too thick and well incorporate the PS. This non-comprehensive list of challenges shows that the design of applicable and efficient

UCNP-PS PDTx agents is everything but simple and necessitates a sophisticated design of PS, UCNP, and their nanohybrid combination.

Keeping the list of challenges in mind, our ideal material list consisted of two recently developed heavy-metal free PS molecules (DBI and TCI) with high $^1\text{O}_2$ production quantum yields (between 74% and 86%) and three different functional groups (aliphatic, hexyl, and maleimide) combined with PLB-coated Nd^{3+} and Yb^{3+} co-doped small (<20 nm) UCNPs with thin inert shells. The organic PS could be directly attached to the inorganic UCNPs via the maleimide group or incorporated in the PLB via the aliphatic or hexyl groups. These two strategies allowed us to evaluate both UCNP-to-PS distance and PS-per-UCNP valence and we found overall FRET efficiencies between 11% and 42% and PS-per-UCNP ratios between 3.1 and 6.2. Ideal PDT functionality consisting of NIR (980 or 808 nm) excitation of UCNPs, UCNP-to-PS FRET, and PS-mediated $^1\text{O}_2$ production was experimentally demonstrated on HeLa cells with cell viabilities down to $\approx 10\%$ and negligible dark cytotoxicity. The intracellular PDT effect, which most probably led to apoptosis and cell death, could be directly monitored via NIR-excited live cell imaging of the UCNP PL, demonstrating the combined therapeutic and diagnostic PDTx applicability. Preliminary in vivo experiments with direct UCNP-PS injection into subcutaneously implanted tumors did not result in tumor size reduction, most probably due to inefficient cellular penetration under the significantly different direct-tumor-injection conditions. However, the in vivo results provided a good guideline for optimizing both the UCNPs and in vivo delivery conditions for a detailed future in vivo study toward clinical translation of our heavy-metal-free sub-20 nm UCNP-PS.

Our results show that careful engineering of molecular and nanomaterials into biocompatible and stable nanohybrid systems can be exploited to design and apply advanced PDTx agents that provide deep tissue penetration via NIR excitation, efficient cellular uptake, high PDT efficacy, and in situ diagnostics via PL imaging. Such nanophotosensitizers have the potential to significantly advance PDTx and considering our successful live-cell proof-of-concept and preliminary in vivo results, we are confident that future investigations will also demonstrate the in vivo PDTx applicability and efficacy of our UCNP-PS nanohybrids.

Supporting Information

Supporting Information is available from the Wiley Online Library or from the author.

Acknowledgements

This research was funded by the Région Normandie and the European Union's Horizon 2020 research and innovation program under the Marie Skłodowska-Curie grant agreement no 101034329 (WINNINGNormandy Fellowship Program), Labex SynOrg (ANR-11-LABX-0029), University of Rouen Normandy, Normandy University, INSA Rouen Normandy, the Centre National de la Recherche Scientifique (CNRS), the European Regional Development Fund (ERDF), Institut Carnot I2C, XL-Chem graduate school (ANR-18-EURE-0020 XL CHEM), the Brain Pool program funded by the Ministry of Science and ICT through the National Research Foundation of Korea (2021H1D3A2A02049589), and the Canada Excellence Research

Chairs Program (CERC in Nano-Optical Biosensing and Molecular Diagnostics, CERC-2022-00072). The authors thank the Institute of Condensed Matter Chemistry and Technologies for Energy (ICMATE) at the University of Padova for XRD, TEM, and TGA measurements. D. P. S. and K. M. acknowledge the MITI of the CNRS and the ANR (BTXI-Apogee, ANR-20-CE05-0029) respectively for funding their PhDs program. This work also received financial support under the EUR LUMOMAT project and the Investments for the Future program (ANR-18-EURE-0012).

Conflict of Interest

The authors declare no conflict of interest.

Data Availability Statement

The data that support the findings of this study are available in the supplementary material of this article.

Keywords

dibenzothioxanthene imide, FRET, imaging, nanoparticles, PDT, thiochromenocarbazole imide

Received: June 12, 2024

Revised: June 19, 2024

Published online:

- [1] P. Agostinis, K. Berg, K. A. Cengel, T. H. Foster, A. W. Girotti, S. O. Gollnick, S. M. Hahn, M. R. Hamblin, A. Juzeniene, D. Kessel, M. Korbelik, J. Moan, P. Mroz, D. Nowis, J. Piette, B. C. Wilson, J. Golab, *CA: Cancer J. Clin.* **2011**, *61*, 250.
- [2] X. Li, J. F. Lovell, J. Yoon, X. Chen, *Nat. Rev. Clin. Oncol.* **2020**, *17*, 657.
- [3] M. R. Hamblin, *Dalton Trans.* **2018**, *47*, 8571.
- [4] J. P. Celli, B. Q. Spring, I. Rizvi, C. L. Evans, K. S. Samkoe, S. Verma, B. W. Pogue, T. Hasan, *Chem. Rev.* **2010**, *110*, 2795.
- [5] R. L. Auten, J. M. Davis, *Pediatr. Res.* **2009**, *66*, 121.
- [6] K. K. Ng, G. Zheng, *Chem. Rev.* **2015**, *115*, 11012.
- [7] M. Prieto, A. Y. Rwei, T. Alejo, T. Wei, M. T. Lopez-Franco, G. Mendoza, V. Sebastian, D. S. Kohane, M. Arruebo, *ACS Appl. Mater. Interfaces* **2017**, *9*, 41737.
- [8] J. Houang, G. G. Perrone, C. Pedrinazzi, L. Longo, D. Mawad, P. C. Boughton, A. J. Ruys, A. Lauto, *Adv. Ther.* **2019**, *2*, 1800105.
- [9] D. Xu, Q. Duan, H. Yu, W. Dong, *J. Mater. Chem. B* **2023**, *11*, 5976.
- [10] Y. Zhao, J. Wang, X. Cai, P. Ding, H. Lv, R. Pei, *ACS Appl. Mater. Interfaces* **2020**, *12*, 23697.
- [11] J. Widengren, C. A. M. Seidel, *Phys. Chem. Chem. Phys.* **2000**, *2*, 3435.
- [12] T. W. Liu, E. Huynh, T. D. MacDonald, G. Zheng, *Cancer Theranostics* **2014**, 229, <https://doi.org/10.1016/B978-0-12-407722-5.00014-1>.
- [13] J. Zhao, K. Chen, Y. Hou, Y. Che, L. Liu, D. Jia, *Org. Biomol. Chem.* **2018**, *16*, 3692.
- [14] V.-N. Nguyen, Y. Yan, J. Zhao, J. Yoon, *Acc. Chem. Res.* **2021**, *54*, 207.
- [15] L. Zhou, F. Wei, J. Xiang, H. Li, C. Li, P. Zhang, C. Liu, P. Gong, L. Cai, K. M.-C. Wong, *Chem. Sci.* **2020**, *11*, 12212.
- [16] L. C.-C. Lee, K. K.-W. Lo, *J. Am. Chem. Soc.* **2022**, *144*, 14420.
- [17] M. Deiana, J. M. Andrés Castán, P. Josse, A. Kahsay, D. P. Sánchez, K. Morice, N. Gillet, R. Ravindranath, A. K. Patel, P. Sengupta, I. Obi, E. Rodriguez-Marquez, L. Khrouz, E. Dumont, L. Abad Galán, M. Allain, B. Walker, H. S. Ahn, O. Maury, P. Blanchard, T. Le Bahers, D. Öhlund, J. von Hofsten, C. MonnerEAU, C. Cabanetos, N. Sabouri, *Nucleic Acids Res.* **2023**, *51*, 6264.

- [18] J. Tang, L. Wang, A. Loredó, C. Cole, H. Xiao, *Chem. Sci.* **2020**, *11*, 6701.
- [19] L. A. Ortiz-Rodríguez, C. E. Crespo-Hernández, *Chem. Sci.* **2020**, *11*, 11113.
- [20] J. M. Andrés Castán, C. Amruth, P. Josse, L. A. Galan, P. S. Marqués, M. Allain, O. Maury, T. L. Bahers, P. Blanchard, C. Monnereau, G. C. Welch, C. Cabanetos, *Mater. Chem. Front.* **2022**, *6*, 1912.
- [21] J. M. Andrés Castán, S. Abidi, T. Ghanem, S. Touihri, P. Blanchard, G. C. Welch, Y. Zagranjarski, J. Boixel, B. Walker, P. Josse, C. Cabanetos, *Colorants* **2023**, *2*, 22.
- [22] H. Zhang, G. Ren, W. Hou, L. Wang, Y. Sun, J. Liu, *Spectrochim. Acta A Mol. Biomol. Spectrosc.* **2024**, *308*, 123688.
- [23] T. Zhang, J. Zhang, F.-B. Wang, H. Cao, D. Zhu, X. Chen, C. Xu, X. Yang, W. Huang, Z. Wang, J. Wang, Z. He, Z. Zheng, J. W. Y. Lam, B. Z. Tang, *Adv. Funct. Mater.* **2022**, *32*, 2110526.
- [24] D. Li, X. Chen, D. Wang, H. Wu, H. Wen, L. Wang, Q. Jin, D. Wang, J. Ji, B. Z. Tang, *Biomaterials* **2022**, *283*, 121476.
- [25] M. Raab, A. Skripka, J. Bulmahn, A. Pliss, A. Kuzmin, F. Vetrone, P. Prasad, *ACS Appl. Bio Mater.* **2022**, *5*, 4948.
- [26] F. Auzel, *Chem. Rev.* **2004**, *104*, 139.
- [27] G. Chen, H. Qiu, P. N. Prasad, X. Chen, *Chem. Rev.* **2014**, *114*, 5161.
- [28] A. Gnach, T. Lipinski, A. Bednarkiewicz, J. Rybka, J. A. Capobianco, *Chem. Soc. Rev.* **2015**, *44*, 1561.
- [29] X. Liu, C.-H. Yan, J. A. Capobianco, *Chem. Soc. Rev.* **2015**, *44*, 1299.
- [30] N. M. Idris, M. K. G. Jayakumar, A. Bansal, Y. Zhang, *Chem. Soc. Rev.* **2015**, *44*, 1449.
- [31] S. He, N. J. J. Johnson, V. A. Nguyen Huu, Y. Huang, A. Almutairi, *Chem. Mater.* **2018**, *30*, 3991.
- [32] C. A. Valle del, T. Hirsch, M. J. Marín, *Methods Appl. Fluoresc.* **2022**, *10*, 034003.
- [33] J. C. Brandmeier, K. Raiko, Z. Farka, R. Peltomaa, M. J. Mickert, A. Hlaváček, P. Skládal, T. Soukka, H. H. Gorris, *Adv. Healthcare Mater.* **2021**, *10*, 2100506.
- [34] N. Rajil, S. Esmaeil, B. W. Neuman, R. Nessler, H.-J. Wu, Z. Yi, R. W. Brick, A. V. Sokolov, P. R. Hemmer, M. O. Scully, *Sci. Rep.* **2022**, *12*, 1263.
- [35] K. Raiko, A. Lyytikäinen, M. Ekman, A. Nokelainen, S. Lahtinen, T. Soukka, *Clin. Chim. Acta* **2021**, *523*, 380.
- [36] N. Bogdan, F. Vetrone, G. A. Ozin, J. A. Capobianco, *Nano Lett.* **2011**, *11*, 835.
- [37] Y. Fan, F. Zhang, *Adv. Opt. Mater.* **2019**, *7*, 1801417.
- [38] S. Bhuckory, S. Lahtinen, N. Höysniemi, J. Guo, X. Qiu, T. Soukka, N. Hildebrandt, *Nano Lett.* **2023**, *23*, 2253.
- [39] L. Francés-Soriano, N. Estebanez, J. Pérez-Prieto, N. Hildebrandt, *Adv. Funct. Mater.* **2022**, *32*, 2201541.
- [40] J. Xu, P. Yang, M. Sun, H. Bi, B. Liu, D. Yang, S. Gai, F. He, J. Lin, *ACS Nano* **2017**, *11*, 4133.
- [41] J. Zhou, N. Shirahata, H.-T. Sun, B. Ghosh, M. Ogawara, Y. Teng, S. Zhou, R. G. Sa Chu, M. Fujii, J. Qiu, *J. Phys. Chem. Lett.* **2013**, *4*, 402.
- [42] S. Hao, G. Chen, C. Yang, W. Shao, W. Wei, Y. N. Liu, P. Prasad, *Nanoscale* **2017**, *9*, 10633.
- [43] F. Pini, L. Francés-Soriano, V. Andriago, M. M. Natile, N. Hildebrandt, *ACS Nano* **2023**, *17*, 4971.
- [44] S. T. Dibaba, X. Ge, W. Ren, L. Sun, *J. Rare Earths* **2019**, *37*, 791.
- [45] M. Matulionyte, A. Skripka, A. Ramos-Guerra, A. Benayas, F. Vetrone, *Chem. Rev.* **2022**, *123*, 515.
- [46] Y.-F. Wang, G.-Y. Liu, L.-D. Sun, J.-W. Xiao, J.-C. Zhou, C.-H. Yan, *ACS Nano* **2013**, *7*, 7200.
- [47] J. Wu, S. Du, Y. Wang, *J. Mater. Chem. B* **2019**, *7*, 7306.
- [48] C. Wang, L. Cheng, Z. Liu, *Theranostics* **2013**, *3*, 317.
- [49] Y. Wang, Y. Li, Z. Zhang, L. Wang, D. Wang, B. Z. Tang, *Adv. Mater.* **2021**, *33*, 2103748.
- [50] G. Jin, R. He, Q. Liu, M. Lin, Y. Dong, K. Li, B. Z. Tang, B. Liu, F. Xu, *Theranostics* **2019**, *9*, 246.
- [51] D. Mao, F. Hu, Z. Yi, Kenry, S. Xu, S. Yan, Z. Luo, W. Wu, Z. Wang, D. Kong, X. Liu, B. Liu, *Sci. Adv.* **2020**, *6*, eabb2712.
- [52] A. D. Hendsbee, J.-P. Sun, W. K. Law, H. Yan, I. G. Hill, D. M. Spasyuk, G. C. Welch, *Chem. Mater.* **2016**, *28*, 7098.
- [53] Y. Dong, B. Dick, J. Zhao, *Org. Lett.* **2020**, *22*, 5535.
- [54] N. Hildebrandt, in *FRET—Förster Resonance Energy Transfer*, (Eds.: I. L. Medintz, N. Hildebrandt), Wiley, Weinheim, **2013**.
- [55] F. Pini, L. Francés-Soriano, N. Peruffo, A. Barbon, N. Hildebrandt, M. M. Natile, *ACS Appl. Mater. Interfaces* **2022**, *14*, 11883.
- [56] J. A. Damasco, G. Chen, W. Shao, H. Ågren, H. Huang, W. Song, J. F. Lovell, P. N. Prasad, *ACS Appl. Mater. Interfaces* **2014**, *6*, 13884.
- [57] N. J. J. Johnson, S. He, V. A. Nguyen Huu, A. Almutairi, *ACS Nano* **2016**, *10*, 8299.
- [58] A. Noculak, A. Podhorodecki, G. Pawlik, M. Banski, J. Misiewicz, *Nanoscale* **2015**, *7*, 13784.
- [59] T. Rinkel, J. Nordmann, A. N. Raj, M. Haase, *Nanoscale* **2014**, *6*, 14523.
- [60] T. Rinkel, A. N. Raj, S. Dühnen, M. Haase, *Angew. Chem., Int. Ed.* **2016**, *55*, 1164.
- [61] S. Tan, X. Li, Y. Guo, Z. Zhang, *Nanoscale* **2013**, *5*, 860.
- [62] P. Thanasekaran, C.-H. Chu, S.-B. Wang, K.-Y. Chen, H.-D. Gao, M. M. Lee, S.-S. Sun, J.-P. Li, J.-Y. Chen, J.-K. Chen, Y.-H. Chang, H.-M. Lee, *ACS Appl. Mater. Interfaces* **2019**, *11*, 84.
- [63] S. Märkl, A. Schroter, T. Hirsch, *Nano Lett.* **2020**, *20*, 8620.
- [64] C. A. Davis, K. McNeill, E. M.-L. Janssen, *Environ. Sci. Technol.* **2018**, *52*, 9908.
- [65] M. J. Weber, *Phys. Rev. B* **1971**, *4*, 3153.
- [66] J. Shen, G. Chen, A.-M. Vu, W. Fan, O. S. Bilsel, C.-C. Chang, G. Han, *Adv. Opt. Mater.* **2013**, *1*, 644.
- [67] P. Mroz, A. Yaroslavsky, G. B. Kharkwal, M. R. Hamblin, *Cancers* **2011**, *3*, 2516.
- [68] D. Kessel, N. L. Oleinick, *Photochem. Photobiol.* **2018**, *94*, 213.
- [69] K. Susumu, E. Oh, J. B. Delehanty, J. B. Blanco-Canosa, B. J. Johnson, V. Jain, W. J. I. Hervey, W. R. Algar, K. Boeneman, P. E. Dawson, I. L. Medintz, *J. Am. Chem. Soc.* **2011**, *133*, 9480.
- [70] S. Behzadi, V. Serpooshan, W. Tao, M. A. Hamaly, M. Y. Alkawareek, E. C. Dreaden, D. Brown, A. M. Alkilany, O. C. Farokhzad, M. Mahmoudi, *Chem. Soc. Rev.* **2017**, *46*, 4218.
- [71] P. Tiefenboeck, J. A. Kim, J.-C. Leroux, *Adv. Drug Delivery Rev.* **2018**, *132*, 3.
- [72] P. R. Ogilby, *Chem. Soc. Rev.* **2010**, *39*, 3181.
- [73] 8 Key Takeaways Of The Proposed FDA Modernization Act 3.0, <https://www.drugdiscoveryonline.com/doc/key-takeaways-of-the-proposed-fda-modernization-act-3-0-0001>, (accessed: March 2024).
- [74] J. Zuo, L. Tu, Q. Li, Y. Feng, I. Que, Y. Zhang, X. Liu, B. Xue, L. J. Cruz, Y. Chang, H. Zhang, X. Kong, *ACS Nano* **2018**, *12*, 3217.
- [75] W. Jiang, C. Zhang, A. Ahmed, Y. Zhao, Y. Deng, Y. Ding, J. Cai, Y. Hu, *Adv. Healthcare Mater.* **2019**, *8*, 1900972.
- [76] B. Zheng, D. Zhong, T. Xie, J. Zhou, W. Li, A. Ilyas, Y. Lu, M. Zhou, R. Deng, *Chem* **2021**, *7*, 1615.
- [77] D. E. Hudson, D. O. Hudson, J. M. Winingar, B. D. Richardson, *Photomed. Laser Surg.* **2013**, *31*, 163.
- [78] T. Li, C. Xue, P. Wang, Y. Li, L. Wu, *J. Innov. Opt. Health Sci.* **2017**, *10*, 1743002.
- [79] H. J. Wei, D. Xing, B. H. He, H. M. Gu, G. Y. Wu, X. M. Chen, *BMC Gastroenterol.* **2009**, *9*, 64.
- [80] T. Cheng, R. Marin, A. Skripka, F. S. Vetrone, B. L.-B. U. Nanoparticles, *J. Am. Chem. Soc.* **2018**, *140*, 12890.
- [81] A. Skripka, T. Cheng, C. M. S. Jones, R. Marin, J. Marques-Hueso, F. Vetrone, *Nanoscale* **2020**, *12*, 17545.
- [82] A. Drozdowski, N. Jurga, D. Przybylska, J. C. Brandmeier, Z. Farka, H. H. Gorris, T. Grzyb, *J. Colloid Interface Sci.* **2023**, *649*, 49.
- [83] X. Zhang, M. Wang, J. Ding, D. Gao, Y. Shi, X. Song, *CrystEngComm* **2012**, *14*, 8357.